



Performance optimization of tandem organic solar cells at varying incident angles based on optical analysis method

XUENAN ZHAO,¹ RUOXI XIA,² HONGGANG GU,^{1,3}  XIANHUA KE,¹ YATING SHI,¹ XIUGUO CHEN,¹  HAO JIANG,¹  HIN-LAP YIP,^{2,4} AND SHIYUAN LIU^{1,5} 

¹State Key Laboratory of Digital Manufacturing Equipment and Technology, Huazhong University of Science and Technology, Wuhan, Hubei 430074, China

²Institute of Polymer Optoelectronic Materials and Devices State Key Laboratory of Luminescent Materials and Devices, South China University of Technology, Guangzhou, Guangdong 510640, China

³hongganggu@hust.edu.cn

⁴msangusyip@scut.edu.cn

⁵shyliu@hust.edu.cn

Abstract: Tandem organic solar cells (OSCs) show great potential due to advantages such as the utilization of wide-spectrum light and low thermalization loss. The current mismatch between sub-cells is one of the major issues reducing the final output efficiency of a tandem device. In this paper, we focus on the current mismatch of tandem OSCs at oblique incidence and aim to reduce its adverse effect on the performances of realistic devices working at varying incident angle. Firstly, we propose an optical analysis method based on the 4×4 matrix formalism to analyze and optimize the performance of tandem solar cells at arbitrary incident angles. Compared with those optimal designs via matching the currents of sub-cells only at normal incidence, the proposed method chooses the optimal structure of the tandem device by maximizing the generated energy density per day with considering the current match at different incident angles during daytime. With the proposed method, a typical tandem organic solar cell is optimized as an example, and the optimized tandem device has a balanced current match at all incident angles during a whole day. Experimental results demonstrate that the generated energy density per day of the optimized tandem device has increased by 4.9% compared to the conventional device optimized only at normal incidence. The proposed method and results are expected to provide some new insights for the performance analysis and optimization of tandem or multi-junction solar cells, especially those devices exhibiting serious current mismatch between sub-cells at varying incident angles in practical applications.

© 2020 Optical Society of America under the terms of the [OSA Open Access Publishing Agreement](#)

1. Introduction

Organic solar cells (OSCs) have gained great attentions in recent years due to some distinct advantages such as low cost, good mechanical flexibility, and solution processable [1–4]. However, the performance of OSCs is mainly limited by the insufficient absorption of the sunlight, due to the narrow absorption range and low charge mobility of organic materials [5,6]. The tandem OSC is an effective means to overcome the above limitation of a single solar cell [7–10]. It can reduce the thermalization loss and increase the efficiency limit of the tandem cell via two or more sub-cells absorbing photons over much wider spectral range. In the tandem cell, all the sub-cells are electrically connected in series, therefore the current output of the tandem device is limited by the smallest current in sub-cells according to Kirchhoff's law [11]. The current mismatch between sub-cells in a tandem device affects the final output efficiency significantly and needs to be controlled and reduced to minimize the energy loss [12,13]. The device architectures,

especially thicknesses of the active layers affect the performance and current matching of the tandem device substantially. As a result, the performance analysis and architecture optimization are critical to improve the performance of the tandem OSCs [14–16].

The optical analysis is a powerful tool to provide accurate predictions for the device performance and guide the optimization of device architectures, and has been widely used in OSCs [15–20]. Chen *et al.* fabricated high efficiency tandem OSCs with the guidance of optical optimization based on the transfer matrix method (TMM), and the structure was optimized by adjusting the two active thicknesses to match the photocurrents in sub-cells of the tandem device at normal incidence [20,21]. Zhang *et al.* applied the optical optimization method to obtain high-performance polymer tandem OSCs by adjusting the active layer thicknesses of front and back sub-cells [22,23]. Some other researchers also focused on the control of current matching in different types of tandem solar cells to improve the device efficiency by optimizing the thicknesses of active layers and spacer layers [11–13]. Although the above researches have achieved high-performance and high-efficiency tandem devices via maximizing the photocurrent of devices and matching the currents of sub-cells according to optical analysis results, they usually optimize the device structures only at normal incidence. In practical applications, the solar cells are often illuminated by sunlight at varying incident angles during daytime, and currents in sub-cells would be no longer matched when light is incident obliquely. Some researchers have paid attentions to the influence of incident angle on the performance of OSCs [24–28]. Inganäs *et al.* suggested that for solar cells working under non-normal incident light, investigation about the device performance at oblique incidence is necessary, and a numerical study about the behavior of tandem OSCs at oblique incidence has been presented based on the finite element method [26]. Kim *et al.* presented a series of studies about the effect of incident angle on single-junction OSCs by optical analysis method based on the TMM [27–29]. They proposed a more practical optimization method to optimize the thickness of active layer in single-junction OSCs by considering the varying incident angles during daytime, and put forward the generated energy density per day as the optimization target. However, there is not yet a comprehensive research about the performance variation and the current mismatch between sub-cells in tandem OSCs by taking the varying incident angles during daytime into account. In addition, the optical anisotropy has been found in various organic materials, and has been confirmed to affect the performance of device significantly [30,31]. Existing researches about the optical analysis and optical optimization for OSCs based on the TMM are difficult to deal with the optical anisotropy.

In this paper, we proposed an optical analysis method to analyze and optimize the performance of tandem solar cells at arbitrary incident angles. An optical model for complex multi-layer devices containing incoherent layers and anisotropic layers is constructed based on the 4×4 matrix formalism. With the proposed method, the tandem structure is optimized by choosing the maximum generated energy density per day with considering the current match at different incident angles during daytime. Simulations and experiments are both carried out about a typical tandem OSC to verify the proposed method. Results demonstrate that the sub-cells have a much more balanced current match when the tandem device work at different incident angles and the generated energy density per day is significantly improved compared to the conventional devices optimized only at normal incidence.

2. Theory and methods

2.1. Optical model of anisotropic multi-layers based on 4×4 matrix method

Figure 1 shows a typical structure of a multi-layer device containing m layers, consisting of an incoherent substrate and several coherent layers between the semi-infinite transparent ambients on the top ($j=0$.) and bottom ($j=m+1$). Each layer j ($j=1,2,\dots,m$) has a thickness d_j and complex refractive indices in x, y and z directions ($N_{xj} = n_{xj} + i\kappa_{xj}$, $N_{yj} = n_{yj} + i\kappa_{yj}$, $N_{zj} = n_{zj} + i\kappa_{zj}$), where n_j and κ_j are refractive index and extinction coefficient, respectively. We assume that the

unpolarized light propagate from the top ambient ($j = 0$) at the angle of θ_0 and transmitted at angle θ_j in the j -th layer. We consider the thick glass substrate ($j = 1$) as an incoherent layer because that its thickness ($\sim 700 \mu\text{m}$) is much larger than the coherence length of sunlight ($\sim 0.6 \mu\text{m}$) [32], while the remaining $m - 1$ layers with thin thicknesses are regarded as coherent layers.

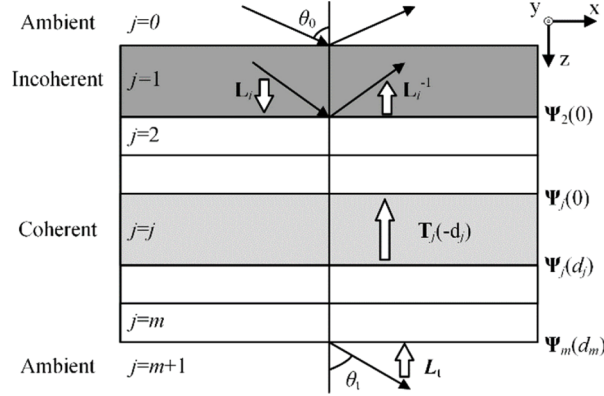


Fig. 1. Schematic diagram of multi-layer structure of the OSC.

For coherent layers, we can get a transfer matrix \mathbf{T}_c to describe the relation between the electric field amplitude in the glass substrate ($j = 1$) and the transmission ambient ($j = m + 1$) based on the 4×4 matrix method [33–35]:

$$\begin{bmatrix} E_{is} & E_{rs} & E_{ip} & E_{rp} \end{bmatrix}^T = \mathbf{T}_c \begin{bmatrix} E_{ts} & 0 & E_{tp} & 0 \end{bmatrix}^T, \quad (1)$$

$$\mathbf{T}_c = \mathbf{L}_i^{-1} \prod_{j=2}^{m1} \mathbf{T}_{jp}(-d_j) \mathbf{L}_t,$$

where E_{is} , E_{ip} , E_{rs} , E_{rp} , E_{ts} , E_{tp} are electric field amplitude of incident, reflected, transmitted s- and p-polarized light for the coherent multi-layers, respectively. The partial transfer matrix of the j -th layer $\mathbf{T}_{jp}(-d_j)$, incident matrix \mathbf{L}_i and exit matrix \mathbf{L}_t are defined by

$$\begin{aligned} \mathbf{L}_i \begin{bmatrix} E_{is} & E_{rs} & E_{ip} & E_{rp} \end{bmatrix}^T &= \Psi_2(0), \\ \mathbf{L}_t \begin{bmatrix} E_{ts} & 0 & E_{tp} & 0 \end{bmatrix}^T &= \Psi_m(d_m), \\ \Psi_j(0) &= \mathbf{T}_{jp}(-d_j) \Psi_j(d_j). \end{aligned} \quad (2)$$

Here, Ψ is a vector containing electric field component \mathbf{E} and magnetic field component \mathbf{H} ,

$$\Psi = \begin{bmatrix} E_x & E_y & H_x & H_y \end{bmatrix}^T. \quad (3)$$

According to the transfer matrix \mathbf{T}_c , transmission and reflection coefficients (r , t), transmittance T_{gm} and reflectance R_{gm} from glass to the multi-layers can be obtained,

$$\begin{aligned} r_{pp} &= \left(\frac{E_{rp}}{E_{ip}} \right)_{E_{is}=0} = \frac{T_{e11}T_{e43} - T_{e13}T_{e41}}{T_{e11}T_{e33} - T_{e13}T_{e31}}, \\ r_{sp} &= \left(\frac{E_{rs}}{E_{ip}} \right)_{E_{is}=0} = \frac{T_{e11}T_{e23} - T_{e13}T_{e21}}{T_{e11}T_{e33} - T_{e13}T_{e31}}, \\ r_{ss} &= \left(\frac{E_{rs}}{E_{is}} \right)_{E_{ip}=0} = \frac{T_{e21}T_{e33} - T_{e23}T_{e31}}{T_{e11}T_{e33} - T_{e13}T_{e31}}, \\ r_{ps} &= \left(\frac{E_{rp}}{E_{ip}} \right)_{E_{is}=0} = \frac{T_{e33}T_{e41} - T_{e31}T_{e43}}{T_{e11}T_{e33} - T_{e13}T_{e31}}, \end{aligned} \quad (4)$$

$$\begin{aligned}
 t_{sp} &= \left(\frac{E_{is}}{E_{ip}}\right)E_{is=0} = \frac{-T_{c13}}{T_{c11}T_{c33}-T_{c13}T_{c31}}, \\
 t_{ss} &= \left(\frac{E_{is}}{E_{is}}\right)E_{ip=0} = \frac{T_{c33}}{T_{c11}T_{c33}-T_{c13}T_{c31}}, \\
 t_{pp} &= \left(\frac{E_{ip}}{E_{ip}}\right)E_{is=0} = \frac{T_{c11}}{T_{c11}T_{c33}-T_{c13}T_{c31}}, \\
 t_{ps} &= \left(\frac{E_{ip}}{E_{is}}\right)E_{ip=0} = \frac{-T_{c31}}{T_{c11}T_{c33}-T_{c13}T_{c31}},
 \end{aligned} \tag{5}$$

$$\begin{aligned}
 R_{gm-s} &= |r_{sp} + r_{ss}|^2, \\
 R_{gm-p} &= |r_{pp} + r_{ps}|^2,
 \end{aligned} \tag{6}$$

$$\begin{aligned}
 T_{gm-s} &= \frac{N_{m+1} \cos(\theta_{m+1})}{N_1 \cos(\theta_1)} |t_{sp} + t_{ss}|^2, \\
 T_{gm-p} &= \frac{N_{m+1} \cos(\theta_{m+1})}{N_1 \cos(\theta_1)} |t_{pp} + t_{ps}|^2.
 \end{aligned} \tag{7}$$

For example, r_{sp} represents the reflected s-polarization (E_{rs}) generated by the incident p-polarization (E_{ip}) when there is no incident s-polarization ($E_{is} = 0$).

Then the electric field intensity traveling through the coherent layers can be de given

$$\begin{bmatrix} U_{is} & U_{rs} & U_{ip} & U_{rp} \end{bmatrix}^T = \overline{\mathbf{T}}_c \begin{bmatrix} U_{ts} & 0 & U_{tp} & 0 \end{bmatrix}^T. \tag{8}$$

Here, $U = |E|^2$ represents the electrical field intensity; $\overline{\mathbf{T}}_c$ is the intensity matrix, which can be obtained by the transfer matrix \mathbf{T}_c .

For the incoherent glass substrate, the coherence is lost due to the thick thickness. Consequently, the optical field intensity rather than optical field amplitude should be taken into account. The electric field intensity at the air/glass interface and in the glass substrate can be described with the intensity matrices, similar to the modified intensity matrix in the generalized transfer matrix method (GTMM) [36]:

$$\begin{bmatrix} U_{0is} & U_{0rs} & U_{0ip} & U_{0rp} \end{bmatrix}^T = \overline{\mathbf{I}} \cdot \overline{\mathbf{L}} \begin{bmatrix} U_{is} & U_{rs} & U_{ip} & U_{rp} \end{bmatrix}^T, \tag{9}$$

where, U_{0is} , U_{0rs} , U_{0ip} , U_{0rp} are electric field intensity of incident, reflected s- and p-polarized light for the total device respectively, $\overline{\mathbf{I}}$ and $\overline{\mathbf{L}}$ are the intensity matrices describing the variation of the electric field intensity at the air/glass interface and in the glass substrate, respectively

$$\overline{\mathbf{I}} = \begin{bmatrix} \overline{\mathbf{I}}_s & 0 \\ 0 & \overline{\mathbf{I}}_p \end{bmatrix}, \overline{\mathbf{I}}_{s(p)} = \frac{1}{|t_{ag-s(p)}|^2} \begin{bmatrix} 1 & -|r_{ga-s(p)}|^2 \\ |r_{ag-s(p)}|^2 & |t_{ag-s(p)}t_{ga-s(p)}|^2 - |r_{ag-s(p)}r_{ga-s(p)}|^2 \end{bmatrix}, \tag{10}$$

$$\overline{\mathbf{L}} = \begin{bmatrix} \overline{\mathbf{L}}_s & 0 \\ 0 & \overline{\mathbf{L}}_p \end{bmatrix}, \overline{\mathbf{L}}_s = \overline{\mathbf{L}}_p = \begin{bmatrix} |e^{-i\beta_g d_g}|^2 & 0 \\ 0 & |e^{i\beta_g d_g}|^2 \end{bmatrix}, \tag{11}$$

where r_{ag} , r_{ga} , t_{ag} and t_{ga} are the front-reflection, back-reflection, front-transmission and back-transmission coefficients at the interface of air and the glass substrate, the subscript s(p) represents the s(p) polarization, $\beta_g = (2\pi/\lambda)N_g$ is the propagation constant in the glass substrate, and d_g is the thickness of substrate.

The total intensity matrix of the whole multi-layer device $\overline{\mathbf{T}}$ is

$$\overline{\mathbf{T}} = \overline{\mathbf{I}} \cdot \overline{\mathbf{L}} \cdot \overline{\mathbf{T}}_c. \tag{12}$$

Then the total transmittance and reflectance of the whole multi-layer device R_{tot} and T_{tot} can be obtained from $\overline{\mathbf{T}}$. When we describe the optical power density distribution in the j -th layer, the

electric field amplitude in the substrate (E_{is} , E_{ip} , E_{rs} , E_{rp}) should be determined first,

$$\begin{aligned} E_{is(p)} &= \sqrt{\frac{T_{s(p)}N_0 \cos(\theta_0)}{T_{gm-s(p)}N_1 \cos(\theta_1)}}, \\ E_{rs} &= E_{is}r_{ss} + E_{ip}r_{sp}, \\ E_{rp} &= E_{is}r_{ps} + E_{ip}r_{pp}. \end{aligned} \tag{13}$$

Then Ψ in the j -th layer can be further described via the incident matrix \mathbf{L}_i and partial transfer matrix \mathbf{T}_{jp} ,

$$\begin{aligned} \begin{bmatrix} E_{is} & E_{rs} & E_{ip} & E_{rp} \end{bmatrix}^T &= \mathbf{L}_i^{-1} \prod_{i=2}^{j-1} \mathbf{T}_{ip}(-d_i) \Psi_j(0), \\ \Psi_j(0) &= \mathbf{T}_{jp}(-z) \Psi_j(z) \quad (0 \leq z \leq d_j), \end{aligned} \tag{14}$$

where $\Psi_j(0)$ and $\Psi_j(d_j)$ are Ψ at the upper and lower surface of the j -th layer, respectively.

The time-average Poynting vector at any position is defined as

$$\begin{aligned} S_{zj}^s(z) &= -\frac{1}{2} \text{Re}\{E_{yj}(z)H_{xj}(z)^*\}, \\ S_{zj}^p(z) &= \frac{1}{2} \text{Re}\{E_{xj}(z)H_{yj}(z)^*\}. \end{aligned} \tag{15}$$

The optical power dissipation is

$$Q_{zj}^{s(p)}(z) = -\frac{dS_{zj}^{s(p)}}{dz}. \tag{16}$$

The photons absorption rate is

$$G = \frac{2\pi\epsilon_0 n \kappa P_{in}}{h} |E|^2, \tag{17}$$

where, P_{in} is the spectral irradiance of the AM 1.5G sunlight, and $|E|^2$ is the electric field intensity.

Finally, the absorptivity of layer j can be written as

$$A_j = \frac{1}{S_0^s} \int_0^{d_j} Q_j^s(z) dz + \frac{1}{S_0^p} \int_0^{d_j} Q_j^p(z) dz. \tag{18}$$

Equations (14)–(18) give the expressions for the optical power flow and absorption characteristics in the multi-layers device containing incoherent layers and anisotropic layers. Thereby, numerical simulations and analysis can be performed on the physical quantities inside the complex multi-layer device by using the proposed model.

2.2. Performance parameters of tandem OSCs at varying incident angles

Based on the above optical model, the performance parameters of any tandem OSCs can be evaluated. The two sub-cells in a tandem OSC are connected in series, thus they have the same current density according to Kirchhoff's law. The short-circuit current J_{sc} of the whole tandem device is smaller than that in the sub-cells,

$$\begin{aligned} J_{SC-f} &= \eta_{IQE} \cdot \int \frac{q\lambda}{hc} P_{in}(\lambda) A_f(\lambda) d\lambda = \eta_{IQE} \cdot q \iint G_f d\lambda dz, \\ J_{SC-r} &= \eta_{IQE} \cdot \int \frac{q\lambda}{hc} P_{in}(\lambda) A_r(\lambda) d\lambda = \eta_{IQE} \cdot q \iint G_r d\lambda dz, \\ J_{SC} &= \min(J_{SC-f}, J_{SC-r}), \end{aligned} \tag{19}$$

where η_{IQE} is the internal quantum efficiency of the device, usually assumed to be 1; q , h , and c are the unit charge, the planck constant and light speed in vacuum, respectively; P_{in} is the spectral

irradiance of the AM 1.5G sunlight; A_f and A_r are absorptance of front and rear active layers respectively; and G_f and G_r refer to the photons absorption rate somewhere in the front and rear active layers.

Also according to Kirchhoff's law, the open-circuit voltage V_{oc} is expressed by

$$V_{oc} = (E_{g-f} + E_{g-r} - E_{loss-f} - E_{loss-r}) / q. \quad (20)$$

Here, E_{g-f} and E_{g-r} are energy bandgap of the two active layers, respectively. E_{loss-f} and E_{loss-r} are the energy loss for the two sub-cells, assumed to be 0.4–0.8eV [20].

According to the calculated short-circuit current J_{sc} and open-circuit voltage V_{oc} in Eqs. (17) and (18), the output electric power density of device is

$$P_{out} = FF \cdot J_{sc} \cdot V_{oc}, \quad (21)$$

where FF is the fill factor.

Considering that the incident angle of sunlight changes during daytime, we optimize the device based on the generation energy density per day, instead of J_{sc} only at normal incidence. We assume that the device is placed at the northern hemisphere with a tilt angle of θ_t , and the light source illuminates at a solar zenith angle of $\theta_z = 48.2^\circ$ according to the definition of AM 1.5G. The tilt angle of device θ_t is usually equal to the solar zenith angle θ_z . The hour angle θ_h indicates the incident angle change of the sun during daytime, and varies at a speed of $15^\circ/h$. We define θ_h is negative in the morning, positive in the afternoon, and zero ($\theta_h = 0^\circ$) at noon (12h). The incidence angle $\theta_0(t)$ is easily expressed by [27]

$$\cos[\theta_0(t)] = \cos(\theta_z - \theta_t) \cos[(t - 12h)15^\circ / h]. \quad (22)$$

The generation energy density per day can be described by

$$E_{day} = \int_{t_{rise}}^{t_{fall}} P(\theta(t)) dt. \quad (23)$$

The above Eqs. (19)–(23) provide the expressions of main parameters for characterizing the device performance. Based on this, the device performance can be evaluated from the simulations.

Furthermore, the variation of the incident angle over a year or a certain period of time can be considered. In this case, the device structure would be optimized according to the generated energy density within a specified time. And the expression of incident angle θ_0 can be represented as

$$\cos \theta_0 = \cos \delta \cos(\phi - \theta_t) \cos \theta_h + \sin \delta \sin(\phi - \theta_t). \quad (24)$$

Here, δ and ϕ are the declination angle and latitude, respectively. In realistic conditions, the declination angle varies in one year and can be calculated on any given day [37]. It should be noted that due to the variation amount of atmosphere that the incident radiation travels through in one year, the irradiation on device P_{in} is not a constant. And to get closer to the realistic conditions, the total irradiation can be further considered as the sum of the direct irradiation, the diffused radiation and reflected radiation [37]. Paetzold *et al.* have provided an energy yield (EY) model with considering the hourly resolved realistic direct and diffuse irradiation conditions as well as cloud cover in different climatic regions, and the EY model was applied to perovskite/silicon multi-junction solar modules [38].

In addition, there are some differences between the measurement conditions in lab and the simulation conditions. As we can see from Fig. 2, the white block in the device indicates the active region of device and is a square with a side length of a . Under measurement conditions in lab in Fig. 2(b), there is a mask with a thickness of d below the device to ensure that only the active areas are illuminated. At normal incidence, the illuminated area is the complete square

($S_0 = a^2$), whether under measurement conditions in lab or simulation conditions. While at oblique incidence, the mask block part of the incident light and the illuminated areas becomes

$$S = a \cdot (a - d \tan \theta). \quad (25)$$

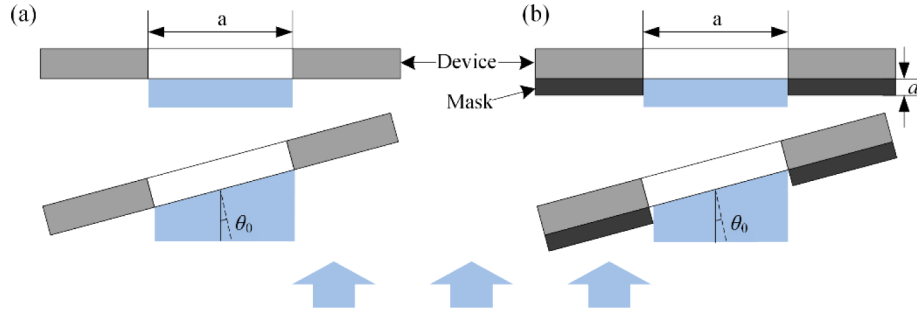


Fig. 2. (a) Simulation conditions without mask. (b) Measurement conditions in lab with mask.

In other words, since part of incident light is blocked by the mask, the illuminated area at oblique incidence in lab is smaller than that in the simulation conditions. Therefore, the performance parameters measured in lab need to be divided by a correction parameter which reflects the difference in the illuminated area. We define the correction parameter α as follows:

$$\alpha = S/S_0 = (a - d \tan \theta)/a. \quad (26)$$

For example, under the measurement condition in lab with $a = 2$ mm and $d = 0.2$ mm, when the light is incident at an angle of 45° , the correction parameter α will be 0.90. Thus, the corrected measured performance parameters become

$$\begin{aligned} J_{SC\text{-exp}}' &= J_{SC\text{-exp}} / \alpha, \\ V_{OC\text{-exp}}' &= V_{OC\text{-exp}}, \\ PCE_{\text{exp}}' &= PCE_{\text{exp}} / \alpha, \\ FF_{\text{exp}}' &= FF_{\text{exp}}. \end{aligned} \quad (27)$$

It should be noted that in realistic conditions, when the substrate is at the front without any mask, there may be some additional light illuminating the area around the cell partially guided to the active area. We have done some experiments and confirmed that the effect of these additional illumination can be negligible.

3. Experiments

3.1. Materials and tandem devices preparations

The tandem OSC structure is shown in Fig. 3(a). The device is composed of glass/ indium tin oxide (ITO)/ poly(3,4-ethylenedioxythiophene):poly(styrenesulfonate) (PEDOT:PSS)/ 5,7-bis(2-ethylhexyl)benzo[1,2-c:4,5-c']dithiophene-4,8-dione (PBDB-T):3,9-bis(4-(1,1-dicyanomethylene)-3-methylene-2-oxo-cyclopenta[b]thiophen)-5,5,11,11-tetrakis(4-hexylphenyl)-dithieno[2,3-d':2,3-d']-s-indaceno[1,2-b:5,6-b']-dithiophene (ITCC)/ poly[(9,9-bis(3'-(N,Ndimethylamino)propyl)-2,7-fluorene)-alt-5,5'-bis(2,2'-thiophene)-2,6-naphthalene-1,4,5,8-tetracarboxylic-N,N'-di

(2-ethylhexyl)imide] (PNDI-F3N)/ Ag/ PEDOT:PSS/ poly[2,60-4,8-di(5-ethylhexylthienyl)benzo[1,2-b;3,3-b[dithiophene]-alt-[3-fluoro-2[(2-ethylhexyl)carbonyl]thieno[3,4-b[thiophenediyl] (PTB7-Th):2,20-((2Z,2'Z)-((4,4,9,9-tetrakis(4-hexylphenyl)-4,9-dihydro-sindaceno[1,2-b:5,6-b']dithiophene-2,7-diyl)bis(4-((2-ethylhexyl)oxy)thiophene-5,2-diyl)bis(methanylylidene))bis(5,6-difluoro-3-oxo-2,3-dihydro-1H-indene-2,1-diylidene))dimalononitrile (IEICO-4F)/ PNDI-F3N/ Ag. A wide bandgap PBDB-T:ITCC [39] sub-cell and a narrow bandgap PTB7-Th:IEICO-4F [40] subcell are chosen to fabricate the tandem OSCs with complementary absorption. We employed PF3N-2TNDI as the electron-transparent-layer (ETL) and PEDOT:PSS as the hole-transparent-layer (HTL) to build the interconnecting layer (ICL). A 2 nm Ag film was evaporated at the ETL/HTL interface to improve the recombination properties.

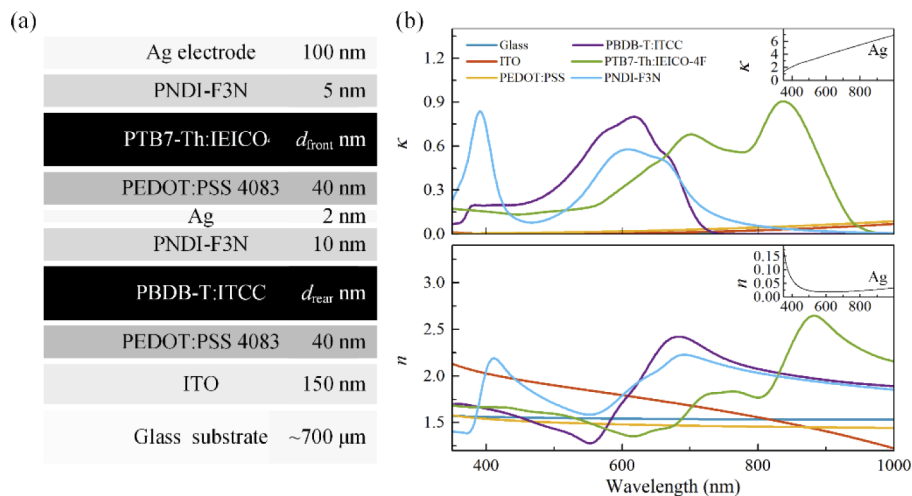


Fig. 3. (a) The device structure of the used tandem OSC; (b) Refractive index (n) and extinction coefficient (κ) of materials employed in the tandem OSC.

The interface material PNDI-F3N [41] were synthesized, and its solution was prepared according to a previously reported procedure. PTB7-Th was purchased from 1-Material Inc. PBDB-T, ITCC, and IEICO-4F were purchased from Solarmer. PEDOT:PSS (Clevios P VP Al 4083) was purchased from Heraeus. Unless otherwise stated, all reagents and solvents were commonly commercially available products and were used as received. Both the PBDB-T:ITCC (w:w = 1:1) and PTB7-Th:IEICO-4F (w:w = 1:1.5) solutions were prepared in a mixed solvent chlorobenzene (CB):1,8-diodooctane (DIO) (v:v = 99.5:0.5 for PBDB-T:ITCC, v:v = 99:1 for PTB7-Th:IEICO-4F).

The fabrication procedure of the tandem OSC device is as follows. The ITO pre-coated glass substrate was ultrasonically cleaned with isopropyl alcohol, deionized water and cleanser essence. After dried in oven, a 40 nm PEDOT:PSS was spin coated onto ITO substrates and baked at 150 °C for 20 min. Then, the blend PBDB-T:ITCC active layer was spin coated onto the PEDOT:PSS film with various thicknesses and thermally annealed at 100 °C for 10 minutes. PNDI-F3N were then spin coated onto PBDB-T:ITCC. After that, 2 nm ultrathin Ag was evaporated onto PNDI-F3N with a base pressure of 1×10^{-7} Torr. Subsequently, 40 nm PEDOT:PSS were spin coated onto ultrathin Ag in atmosphere and baked at 100 °C for 10 min in N_2 protected glove box to remove the residual water. Then, PTB7-Th:IEICO-4F active layer were spin coated onto PEDOT:PSS and baked at 100 °C for 10 min. After that, 5 nm PNDI-F3N was spin coated onto PTB7-Th:IEICO-4F. Devices were at last finished by evaporating 100 nm Ag through a shadow mask (2 mm \times 2 mm active area was defined) in a vacuum chamber with a base pressure of 1×10^{-7} Torr. The thicknesses of the solution processed films are controlled by the spinning

speed and are checked by a broadband spectroscopic Muller matrix ellipsometer (ME-L, Wuhan Eoptics Company) [42,43].

3.2. Materials and device characterization

As shown in Fig. 3(b), the optical constants (including the refractive index n and extinction coefficients κ) of materials used in the tandem device were determined by the spectroscopic ellipsometer over the wavelength range of 350–1650 nm at the multi-incidence measurement mode with the incidence set at 60°, 65°, and 70°. It can be seen from Fig. 3(b) that the bandgap of the front-cell active layer PBDB-T:ITCC is about 1.66 eV, and it mainly absorbs light over the visible range 350–740 nm. While the bandgap of the rear-cell active layer PTB7-Th:IEICO-4F is about 1.25 eV, and it mainly absorbs light over the infrared range 350–1000 nm.

The current density-voltage (J-V) curves were measured on a computer-controlled Keithley 2400 sourcemeter under 1 sun, AM 1.5G spectra from a class solar simulator (Taiwan, Enlitech), the light intensity was 100 mW/cm² as calibrated by a NREL certified reference monocrystal silicon cell (Hamamatsu). Before the J-V test, aperture with precise area of 4 mm² was capped onto devices. In order to measure the angle-dependent performance of the tandem OSCs, we rotated the devices with respect to the fixed light source, as shown in Fig. 4.

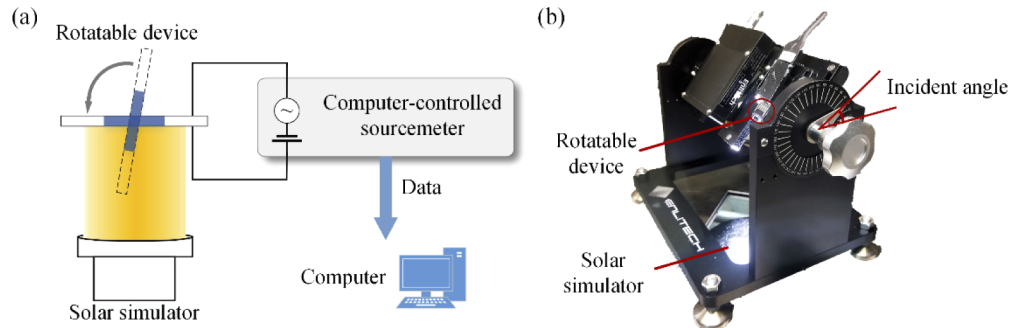


Fig. 4. (a) Schematic and (b) Platform of the experimental set-up for measuring the performance of solar cells at varying incident angles.

4. Results and discussions

4.1. Optimized tandem OSC at normal incidence

Usually, the performance of tandem OSC is optimized by adjusting the thicknesses of two active layers. Thus, we simulated the short-circuit current J_{SC} as a function of thicknesses of the front and rear active layers (d_{front} and d_{rear}) at normal incidence. The d_{front} and d_{rear} are both varied from 5 to 200 nm, and the J_{SC} of device is calculated via integrating the photons absorbed over the wavelength range from 350 to 1000 nm. From the calculated results in Fig. 5, it is obvious that J_{SC} shows the interference oscillation in the variation range of d_{front} and d_{rear} , and J_{SC} reaches a maximum 13.65 mA/cm² when $d_{front} = 140$ nm and $d_{rear} = 100$ nm. Based on the simulation, we fabricated the conventional device optimized at normal incidence (called the conventional device) with 140 nm and 100 nm active layers. In addition, for the purpose of learning the performance of tandem device at oblique incidence, we simulated and measured the conventional device illuminated at different incident angles.

Figure 6 shows the simulated performances of the normal optimized tandem device ($d_{front} = 140$ nm, $d_{rear} = 100$ nm) working at different incident angles. Figure 6(a) shows the photon absorption rate together with its integral over wavelength when the tandem device working at normal incidence. It is clear that the front cell mainly absorbs the photons over the visible region of

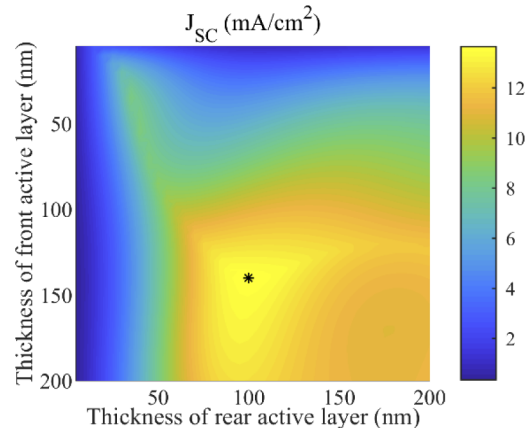


Fig. 5. Simulated J_{sc} generated in the tandem OSC as a function of thicknesses of the front and rear sub-cells at normal incidence. (The asterisk symbol represents the optimal structure.)

350–710 nm, while the rear cell mainly absorbs the photons over the infrared region of 690–950 nm. The J_{sc} of the front cell and rear cell obtained by integrating photons absorbed there are 13.66 mA/cm² and 13.65 mA/cm² respectively, which explain that the J_{sc} of tandem device reaches maximum when the currents of two sub-cells match. Figure 6(b) represents photons absorption rate in sub-cells of the conventional device working at oblique incidence. When the angle of incidence increase, the absorption of photons by two active layers both reduce due to the increased reflection on the air/glass interface. However, the reduction of photons absorption in rear active layer is more than it in front active layer. Correspondingly, J_{sc} generated by front cell is larger than that produced by rear cell as the sun falling (incident angle increasing), as shown in Fig. 6(c). Here, we use the difference between the currents generated in the front and rear sub-cells ($\delta J_{sc} = J_{sc-f} - J_{sc-r}$) to describe the degree of current mismatch, J_{sc-f} and J_{sc-r} refer to short-circuit currents generated by the front and rear sub-cells, respectively.

To study the performance of the conventional device at oblique incidence from the experimental perspective, we prepared devices with 140 nm and 100 nm active layers and measured the device at different incident angles. The incident angle is set varying from 0° to 75°. The measured results are corrected by Eq. (26) ($a = 2$ mm, $d = 0.2$ mm) and are shown in Fig. 7. The corrected J_{sc} data are also plotted in Fig. 6(c) as diamond marks. The calculated and measured J_{sc} both decrease as incident angle increasing and comply with Lambert's cosine law [44], and the measured J_{sc} are lower than the calculated values as a result of internal quantum efficiency assumed to be 100% and neglected device degradation in the simulation. As shown in Fig. 7(a), V_{oc} has a natural logarithm dependence on J_{sc} , which is agree with existing literature [45], and slightly reduced (are almost constant) at the incident angle between 0° to 75°. Figure 7(b) shows the angular response of the experimental power conversion efficiency (PCE) and the experimental fill factor (FF). Due to the reason that V_{oc} and fill factor (FF) are almost constant, PCE shows almost same angular response with J_{sc} .

4.2. Optimized tandem OSC at oblique incidence

As mentioned before, when tandem devices are optimized via matching the currents of two sub-cells, the effect of incident angle on the current matching in tandem devices should also be considered. Therefore, we further simulated J_{sc} as a function of thicknesses of two active layers at oblique incidence. The d_{front} and d_{rear} are both varied from 5 to 200 nm, and incident angle is set as 0°, 15°, 30°, 45°, 60°, 75°. From the calculated results in Fig. 8, it is obvious

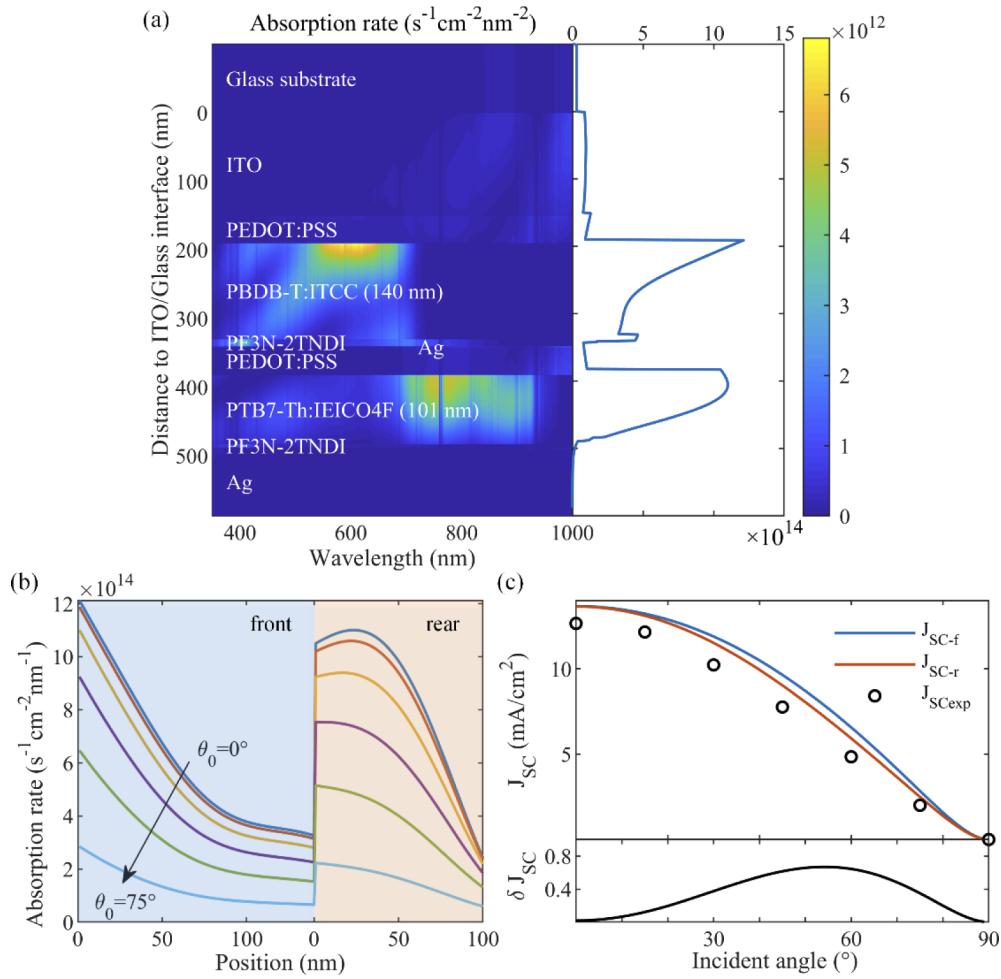


Fig. 6. (a) Simulated absorption rate and its integral over wavelength in the conventional device working at normal incidence; (b) Simulated absorption rate of active layers when the conventional device working at oblique incidence; (c) Simulated J_{SC} in sub-cells and measured J_{SC} of the conventional device at different incident angles. The inset is the simulated current mismatch between two sub-cells in the conventional device.

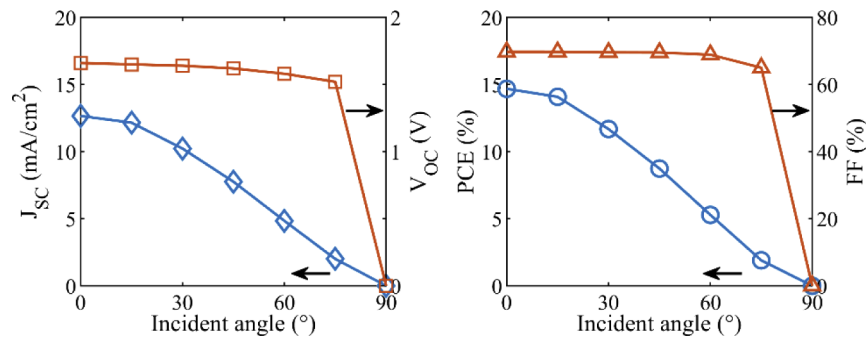


Fig. 7. Corrected experimental performance parameters of the conventional device ($d_{front} = 140$ nm, $d_{rear} = 100$ nm).

that J_{SC} decrease remarkably as a result of enhanced reflected light caused by the increased incident angle. The position of the maximum of J_{SC} in each subgraph indicates the optimal thicknesses at the corresponding incident angle and the detailed data are shown in Table 1. It can be seen that the optimized d_{front} and d_{rear} are not constant at different incident angles. At normal incidence, J_{SC} reaches the maximum 13.65 mA/cm² when $d_{front} = 140$ nm and $d_{rear} = 100$ nm. When incident angle increase to 75°, J_{SC} reaches the maximum 2.69 mA/cm² when $d_{front} = 124$ nm and $d_{rear} = 128$ nm. As the incident angle increasing, the optimized d_{front} decreases gradually, while the optimized d_{rear} increases gradually. And the variation trends of d_{front} and d_{rear} are consistent with Fig. 7(c), as the sun falling (incident angle increasing), the thickness of the front active layer need to decrease and the thickness of the rear active layer need to increase to match the currents in two sub-cells. Moreover, when light is incident obliquely, the J_{SC} of the corresponding optimized device is larger than that of the conventional device, which also proves that varying incident angles from sunrise to sunset has effects on the energy output of the tandem device and should be concerned during optimization process.

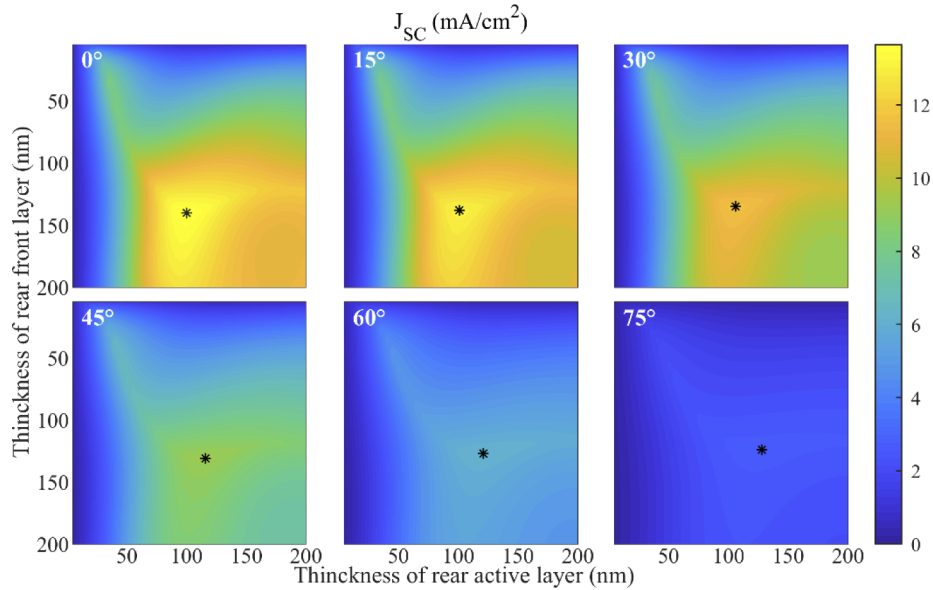


Fig. 8. Simulated J_{SC} generated in the tandem OSC as a function of thickness of the front and rear sub-cells at different incident angles. (The asterisk symbol in each subgraph represents the optimal structure at the corresponding incident angle.)

Table 1. Optimized active layer thicknesses and J_{SC} of tandem device

Incident angle (°)		0	15	30	45	60	75
Optimized thickness (nm)	front	140	138	135	131	127	124
	rear	100	101	106	116	121	128
J_{SC} (mA/cm ²)		13.65	13.14	11.65	9.31	6.26	2.69
J_{SC} of the conventional device (mA/cm ²)		13.65	13.10	11.51	9.03	5.92	2.49

Figure 9 represents the angular response of δJ_{SC} existing in devices optimized at different incident angles. The incident angle varies from 0° to 90°, namely, from noon to sunset. because the incident angle varies linearly with time in Eq. (22) when the device tilts at the solar zenith angle θ_Z ($\theta_t = \theta_Z$), the lateral axis can be regard as a time axis. It can be seen in Fig. 9 that

the δJ_{SC} of each optimized device reaches zero (achieves current match) at its corresponding incident angle. The area enclosed by each curve and the time-axis represents the sum of δJ_{SC} in the homologous device from noon to sunset. As we have mentioned before in Section 4.1, V_{OC} and FF are almost constant at different incident angle. Therefore, according to Eq. (21), the sum of δJ_{SC} can also reflect the power loss per day of the device. It is clear that the energy loss of the conventional device has a large optimization space.

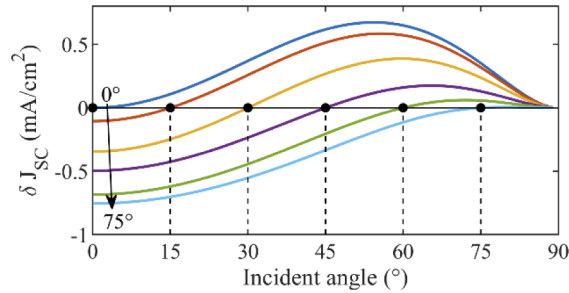


Fig. 9. Angular response of ρJ_{SC} existing in optimized device at different incident angle.

4.3. Optimized tandem OSC considering incident angles variation during daytime

In order to minimize the energy loss and maximize the energy generation of tandem OSCs during daytime, we calculated the generated energy density per day as a function of the thicknesses of the two active layers, and simulation results are shown in Fig. 10. Based on the previous results shown in Sections 4.1 and 4.2, the d_{front} and d_{rear} are set as 90–170 nm and 70–150 nm, respectively. The tilt angle θ_t of the tandem OSC is assumed to be the same as the zenith angle of the sun θ_z , which is 48.2°. In addition, we set the sun to rise at 6:00 and fall at 18:00. V_{oc} is set to 1.62 V and FF is set to 69%, which are obtained from the measurement data in Section 4.1. From the calculated results shown in Fig. 10, similar to the previous results, the generated energy density per day also shows the interference oscillation in the variation ranges of d_{front} and d_{rear} . However, the generated energy density per day reaches its maximum 110.01 mWh/cm² when $d_{front} = 137$ nm, $d_{rear} = 109$ nm. Then we fabricated the optimized tandem device with 135 nm and 110 nm active layers (named all-day optimized device) and measured it at different incident angles to investigate the operation of device from sunrise till sunset.

Figure 11 compares the two optimized devices in terms of simulation results and experimental results. Figure 11(a) displays the current mismatch in two kinds of optimized devices from noon to sunset. The results demonstrate that the current mismatch in all-day optimized device has a smaller mean and is balanced at the different incident angles during daytime compared to the conventional device. The energy loss in the optimized device is approved to be reduced significantly. In addition, the corrected experimental power density in two kinds of optimized devices are shown in Fig. 11(b). According to the linear relationship between incident angle and time, the incident angle changes from -90 degree to 90 degree, which is equivalent to the time varying from sunrise (6:00) to sunset (18:00). It can be seen that although the power density in all-day optimized device is slightly lower than that of the conventional device at normal incidence, when incident light tilts more than about 20°, the performance of all-day optimized device will be better than the conventional device. The areas enclosed by power density curves and time (incident angle) axis represent the generated energy density per day in the corresponding device, the all-day optimized device generates an energy density of 101.06 mWh/cm², which is increased by 4.9% compared to the energy density of 96.32 mWh/cm² generated per day by the conventional device. The above results demonstrate that the proposed optimization method

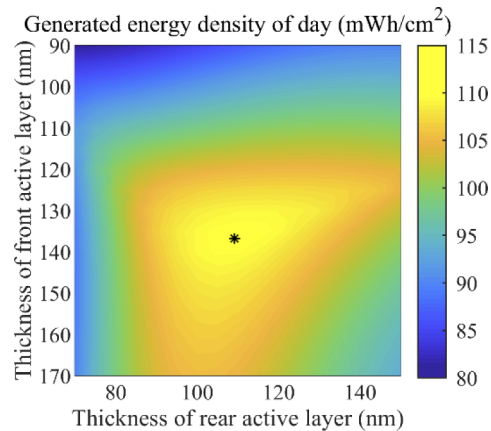


Fig. 10. Simulated generated energy density per day generated in the tandem OSC as a function of thicknesses of the front and rear active layers. (The asterisk symbol represents the optimal structure.)

considering the varying incident angles is superior to the conventional optimization method, and it is important to take into account the effect of the varying incident angles during daytime on the optical analysis and optimization of tandem OSCs.

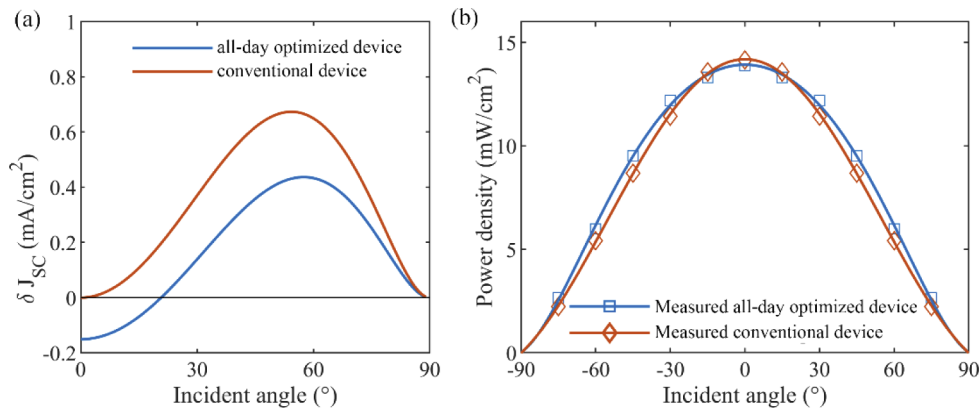


Fig. 11. (a) Calculated δJ_{SC} from noon to sunset and (b) Measured results of the power density during daytime in two kinds of optimized devices

5. Conclusion

In this paper, an optical analysis method has been proposed to analyze and optimize the performance of tandem solar cells at arbitrary incident angles. An optical model is constructed for complex multi-layer structures containing anisotropic layers and incoherent layers by using the 4×4 matrix formulism. Based on the proposed model, the performance parameters, including the short-circuit current, the open-circuit voltage, and the generated energy density, of tandem solar cells are defined and evaluated. The structure of the tandem devices is optimized according to the maximum generated energy density per day with considering the current match at different incident angles during daytime. Numerical simulations and experiments are both carried out on a typical tandem OSC to verify the proposed optical analysis method. The optimized tandem OSC by considering the varying incident angles shows a much more balanced current match at

different incident angles during daytime than the device optimized only at normal incidence. The measured generated energy density per day of the optimized tandem device has increased by 4.9% compared to the conventional device optimized at normal incidence. These results demonstrate the effectiveness and advantage of the proposed method in the performance optimization of tandem or multi-junction solar cells containing complex layers at varying incident angles in practical applications.

Funding

National Natural Science Foundation of China (51525502, 51727809, 51775217, 51805193); China Postdoctoral Science Foundation (2016M602288, 2017T100546); National Major Science and Technology Projects of China (2017ZX02101006-004); Natural Science Foundation of Hubei Province (2018CFA057, 2018CFB559).

Acknowledgments

X. Zhao and R. Xia contributed equally to this work. The authors thank the technical support from the Experiment Center for Advanced Manufacturing and Technology in School of Mechanical Science & Engineering of HUST.

Disclosures

The authors declare no conflicts of interest.

References

1. Z. Xiao, X. Jia, and L. Ding, "Ternary organic solar cells offer 14% power conversion efficiency," *Sci. Bull.* **62**(23), 1562–1564 (2017).
2. S. Zhang, Y. Qin, J. Zhu, and J. Hou, "Over 14% Efficiency in Polymer Solar Cells Enabled by a Chlorinated Polymer Donor," *Adv. Mater.* **30**(20), 1800868 (2018).
3. Y. Lin, J. Wang, Z. G. Zhang, H. Bai, Y. Li, D. Zhu, and X. Zhan, "An electron acceptor challenging fullerenes for efficient polymer solar cells," *Adv. Mater.* **27**(7), 1170–1174 (2015).
4. J. Yuan, Y. Zhang, L. Zhou, G. Zhang, H.-L. Yip, T.-K. Lau, X. Lu, C. Zhu, H. Peng, P. A. Johnson, M. Leclerc, Y. Cao, J. Ulanski, Y. Li, and Y. Zou, "Single-Junction Organic Solar Cell with over 15% Efficiency Using Fused-Ring Acceptor with Electron-Deficient Core," *Joule* **3**(4), 1140–1151 (2019).
5. W. Cao and J. Xue, "Recent progress in organic photovoltaics: device architecture and optical design," *Energy Environ. Sci.* **7**(7), 2123–2144 (2014).
6. C. H. Energy ProcediaHenry, "Limiting efficiencies of ideal single and multiple energy gap terrestrial solar cells," *J. Appl. Phys.* **51**(8), 4494–4500 (1980).
7. X. Che, Y. Li, Y. Qu, and S. R. Forrest, "High fabrication yield organic tandem photovoltaics combining vacuum- and solution-processed subcells with 15% efficiency," *Nat. Energy* **3**(5), 422–427 (2018).
8. P. Cheng, Y. Liu, S.-Y. Chang, T. Li, P. Sun, R. Wang, H.-W. Cheng, T. Huang, L. Meng, S. Nuryyeva, C. Zhu, K.-H. Wei, B. Sun, X. Zhaon, and Y. Yang, "Efficient Tandem Organic Photovoltaics with Tunable Rear Sub-cells," *Joule* **3**(2), 432–442 (2019).
9. G. Liu, J. Jia, K. Zhang, X. Jia, Q. Yin, W. Zhong, L. Li, F. Huang, and Y. Cao, "15% Efficiency Tandem Organic Solar Cell Based on a Novel Highly Efficient Wide-Bandgap Nonfullerene Acceptor with Low Energy Loss," *Adv. Energy Mater.* **9**(11), 1803657 (2019).
10. P. Cheng, G. Li, X. Zhan, and Y. Yang, "Next-generation organic photovoltaics based on non-fullerene acceptors," *Nat. Photonics* **12**(3), 131–142 (2018).
11. M. Bonnet-Eymard, M. Boccard, G. Bugnon, F. Sculati-Meillaud, M. Despeisse, and C. Ballif, "Optimized short-circuit current mismatch in multi-junction solar cells," *Sol. Energy Mater. Sol. Cells* **117**, 120–125 (2013).
12. R. Schueppel, R. Timmreck, N. Allinger, T. Mueller, M. Furno, C. Urich, K. Leo, and M. Riede, "Controlled current matching in small molecule organic tandem solar cells using doped spacer layers," *J. Appl. Phys.* **107**(4), 044503 (2010).
13. Z. Wang, C. Zhang, D. Chen, J. Zhang, Q. Feng, S. Xu, X. Zhou, and Y. Hao, "Investigation of Controlled Current Matching in Polymer Tandem Solar Cells Considering Different Layer Sequences and Optical Spacer," *Jpn. J. Appl. Phys.* **51**(12R), 122301 (2012).
14. X. Zhao, Z. Li, T. Zhu, B. Mi, Z. Gao, and W. Huang, "Structure optimization of organic planar heterojunction solar cells," *J. Phys. D: Appl. Phys.* **46**(19), 195105 (2013).

15. R. Xia, H. Gu, S. Liu, K. Zhang, H.-L. Yip, and Y. Cao, "Optical Analysis for Semitransparent Organic Solar Cells," *Sol. RRL* **3**(1), 1800270 (2019).
16. R. Xia, C. J. Brabec, H.-L. Yip, and Y. Cao, "High-Throughput Optical Screening for Efficient Semitransparent Organic Solar Cells," *Joule* **3**(9), 2241–2254 (2019).
17. G. Zhang, R. Xia, Z. Chen, J. Xiao, X. Zhao, S. Liu, H.-L. Yip, and Y. Cao, "Overcoming Space-Charge Effect for Efficient Thick-Film Non-Fullerene Organic Solar Cells," *Adv. Energy Mater.* **8**(25), 1801609 (2018).
18. L. Song and A. Uddin, "Design of high efficiency organic solar cell with light trapping," *Opt. Express* **20**(S5), A606–A621 (2012).
19. B. Lipovšek, A. Čampa, F. Guo, C. J. Brabec, K. Forberich, J. Krč, and M. Topič, "Detailed optical modelling and light-management of thin-film organic solar cells with consideration of small-area effects," *Opt. Express* **25**(4), A176–A190 (2017).
20. L. Meng, Y. Zhang, X. Wan, C. Li, X. Zhang, Y. Wang, X. Ke, Z. Xiao, L. Ding, R. Xia, H. L. Yip, Y. Cao, and Y. Chen, "Organic and solution-processed tandem solar cells with 17.3% efficiency," *Science* **361**(6407), 1094–1098 (2018).
21. M. Li, K. Gao, X. Wan, Q. Zhang, B. Kan, R. Xia, F. Liu, X. Yang, H. Feng, W. Ni, Y. Wang, J. Peng, H. Zhang, Z. Liang, H.-L. Yip, X. Peng, Y. Cao, and Y. Chen, "Solution-processed organic tandem solar cells with power conversion efficiencies >12%," *Nat. Photonics* **11**(2), 85–90 (2017).
22. K. Zhang, K. Gao, R. Xia, Z. Wu, C. Sun, J. Cao, L. Qian, W. Li, S. Liu, F. Huang, X. Peng, L. Ding, H. L. Yip, and Y. Cao, "High-Performance Polymer Tandem Solar Cells Employing a New n-Type Conjugated Polymer as an Interconnecting Layer," *Adv. Mater.* **28**(24), 4817–4823 (2016).
23. K. Zhang, B. Fan, R. Xia, X. Liu, Z. Hu, H. Gu, S. Liu, H.-L. Yip, L. Ying, F. Huang, and Y. Cao, "Highly Efficient Tandem Organic Solar Cell Enabled by Environmentally Friendly Solvent Processed Polymeric Interconnecting Layer," *Adv. Energy Mater.* **8**(15), 1703180 (2018).
24. A. Meyer and H. Ade, "The effect of angle of incidence on the optical field distribution within thin film organic solar cells," *J. Appl. Phys.* **106**(11), 113101 (2009).
25. A. Mertens, J. Mescher, D. Bahro, M. Koppitz, and A. Colmann, "Understanding the angle-independent photon harvesting in organic homo-tandem solar cells," *Opt. Express* **24**(10), A898–A906 (2016).
26. B. V. Andersson, U. Wuerfel, and O. Inganäs, "Full day modelling of V-shaped organic solar cell," *Sol. Energy* **85**(6), 1257–1263 (2011).
27. S. Lee, I. Jeong, H. P. Kim, S. Y. Hwang, T. J. Kim, Y. D. Kim, J. Jang, and J. Kim, "Effect of incidence angle and polarization on the optimized layer structure of organic solar cells," *Sol. Energy Mater. Sol. Cells* **118**, 9–17 (2013).
28. J. Kim, S. Jung, and I. Jeong, "Optical Modeling for Polarization-dependent Optical Power Dissipation of Thin-film Organic Solar Cells at Oblique Incidence," *J. Opt. Soc. Korea* **16**(1), 6–12 (2012).
29. K. Kang, S. Lee, and J. Kim, "Effect of an Incoherent Glass Substrate on the Absorption Efficiency of Organic Solar Cells at Oblique Incidence Analyzed by the Transfer Matrix Method with a Glass Factor," *Jpn. J. Appl. Phys.* **52**(5R), 052301 (2013).
30. J. Bergqvist, H. Arwin, and O. Inganäs, "Uniaxial Anisotropy in PEDOT:PSS Electrodes Enhances the Photocurrent at Oblique Incidence in Organic Solar Cells," *ACS Photonics* **5**(8), 3023–3030 (2018).
31. M. F. G. Klein, G. Q. G. de Medeiros, P. Kapetana, U. Lemmer, and A. Colmann, "Modeling approach to derive the anisotropic complex refractive index of polymer:fullerene blends for organic solar cells utilizing spectroscopic ellipsometry," *J. Photonics Energy* **5**(1), 057204 (2015).
32. A. Donges, "The coherence length of black-body radiation," *Eur. J. Phys.* **19**(3), 245–249 (1998).
33. H. Fujiwara, *Spectroscopic ellipsometry: principles and applications* (John Wiley & Sons, 2007).
34. M. Schubert, "Polarization-dependent optical parameters of arbitrarily anisotropic homogeneous layered systems," *Phys. Rev. B* **53**(8), 4265–4274 (1996).
35. D. W. Berreman, "Optics in Stratified and Anisotropic Media: 4×4-Matrix Formulation," *J. Opt. Soc. Am.* **62**(4), 502–510 (1972).
36. S. Jung, K.-Y. Kim, Y.-I. Lee, J.-H. Youn, H.-T. Moon, J. Jang, and J. Kim, "Optical Modeling and Analysis of Organic Solar Cells with Coherent Multilayers and Incoherent Glass Substrate Using Generalized Transfer Matrix Method," *Jpn. J. Appl. Phys.* **50**(12R), 122301 (2011).
37. ITACA, "Solar Photovoltaics" (2013), <https://www.itacanet.org/itaca/sections/energy/solar-photovoltaics/>.
38. R. Schmager, M. Langenhorst, J. Lehr, U. Lemmer, B. S. Richards, and U. W. Paetzold, "Methodology of energy yield modelling of perovskite-based multi-junction photovoltaics," *Opt. Express* **27**(8), A507–A523 (2019).
39. H. Yao, L. Ye, J. Hou, B. Jang, G. Han, Y. Cui, G. M. Su, C. Wang, B. Gao, R. Yu, H. Zhang, Y. Yi, H. Y. Woo, H. Ade, and J. Hou, "Achieving Highly Efficient Nonfullerene Organic Solar Cells with Improved Intermolecular Interaction and Open-Circuit Voltage," *Adv. Mater.* **29**(21), 1700254 (2017).
40. H. Yao, Y. Cui, R. Yu, B. Gao, H. Zhang, and J. Hou, "Design, Synthesis, and Photovoltaic Characterization of a Small Molecular Acceptor with an Ultra-Narrow Band Gap," *Angew. Chem., Int. Ed.* **56**(11), 3045–3049 (2017).
41. Z. Wu, C. Sun, S. Dong, X. F. Jiang, S. Wu, H. Wu, H. L. Yip, F. Huang, and Y. Cao, "n-Type Water/Alcohol-Soluble Naphthalene Diimide-Based Conjugated Polymers for High-Performance Polymer Solar Cells," *J. Am. Chem. Soc.* **138**(6), 2004–2013 (2016).
42. S. Liu, X. Chen, and C. Zhang, "Development of a broadband Mueller matrix ellipsometer as a powerful tool for nanostructure metrology," *Thin Solid Films* **584**, 176–185 (2015).

43. H. Gu, X. Chen, H. Jiang, C. Zhang, and S. Liu, "Optimal broadband Mueller matrix ellipsometer using multi-waveplates with flexibly oriented axes," *J. Opt.* **18**(2), 025702 (2016).
44. H. Gross, W. Singer, M. Totzeck, F. Blechinger, and B. Ahtner, *Handbook of optical systems* (Wiley Online Library, 2005), Vol. 1.
45. L. J. A. Koster, V. D. Mihaietchi, R. Ramaker, and P. W. M. Blom, "Light intensity dependence of open-circuit voltage of polymer:fullerene solar cells," *Appl. Phys. Lett.* **86**(12), 123509 (2005).